

Dynamic component of the asthenosphere: lateral viscosity variations due to dislocation creep at the base of oceanic plates

Vojtech Patočka¹, Hana Cizkova², and Jakub Pokorný¹

¹Charles University

²Charles University, Faculty of Mathematics and Physics

April 16, 2024

Abstract

The asthenosphere is commonly defined as an upper mantle zone with low velocities and high attenuation of seismic waves, and high electrical conductivity. These observations are usually explained by the presence of partial melt, or by a sharp contrasts in the water content of the upper mantle. Low viscosity asthenosphere is an essential ingredient of functioning plate tectonics. We argue that a substantial component of asthenospheric weakening is dynamic, caused by dislocation creep at the base of tectonic plates. Numerical simulations of subduction show that dynamic weakening scales with the surface velocity both below the subducting and the overriding plate, and that the viscosity decrease reaches up to two orders of magnitude. The resulting scaling law is employed in an apriori estimate of the lateral viscosity variations (LVV) below Earth's oceans. The obtained LVV helps in explaining some of the long-standing as well as recent problems in mantle viscosity inversions.

Dynamic component of the asthenosphere: lateral viscosity variations due to dislocation creep at the base of oceanic plates

Vojtěch Patočka^a, Hana Čížková^a and Jakub Pokorný^a

^aCharles University, Faculty of Mathematics and Physics, Department of Geophysics, V Holešovičkách 2, 180 00 Prague, Czech Republic

ARTICLE INFO

Keywords:

Asthenosphere
Dislocation creep
Plate tectonics
Mantle viscosity
Subduction
Numerical modeling

ABSTRACT

The asthenosphere is commonly defined as an upper mantle zone with low velocities and high attenuation of seismic waves, and high electrical conductivity. These observations are usually explained by the presence of partial melt, or by a sharp contrasts in the water content of the upper mantle. Low viscosity asthenosphere is an essential ingredient of functioning plate tectonics. We argue that a substantial component of asthenospheric weakening is dynamic, caused by dislocation creep at the base of tectonic plates. Numerical simulations of subduction show that dynamic weakening scales with the surface velocity both below the subducting and the overriding plate, and that the viscosity decrease reaches up to two orders of magnitude. The resulting scaling law is employed in an apriori estimate of the lateral viscosity variations (LVV) below Earth's oceans. The obtained LVV helps in explaining some of the long-standing as well as recent problems in mantle viscosity inversions.

1. Introduction

Defined as a mechanically weak layer that accommodates vertical isostatic movements of Earth's continents, the asthenosphere is originally a geodynamic concept (Barrell, 1914). Later, it was attributed with low velocities and high attenuation of seismic waves (e.g. Dziewonski and Anderson, 1981; Montagner and Tanimoto, 1991), and also with high electrical conductivity (Shankland et al., 1981) – observations typical for the presence of melt, leading to speculations about widespread partial melting in the upper mantle (e.g. Lambert and Wyllie, 1970; Shankland et al., 1981; Mierdel et al., 2007; Hirschmann, 2010). Recently, Hua et al. (2023) showed that the onset of partial melting is visible in receiver function data from globally distributed seismic stations. Karato (2012), however, argues that the origin of the asthenosphere lies elsewhere. He explains the geophysical observations by assuming a sharp change in the water content of the suboceanic mantle. Due to the second-stage partial melting, ascending mantle material becomes dehydrated approximately 70 km below mid-ocean ridges (Morgan and Morgan, 1999), at the same depth at which the 5-10% drop in seismic velocity is observed in old oceanic

plates (e.g. Rychert and Shearer, 2009; Kawakatsu et al., 2009), but where geothermal models predict subsolidus temperatures (i.e., where a sharp contrast in the melt content is unlikely, Fig 5 in Karato, 2012).

A third hypothesis, pursued e.g. by Morgan et al. (2013), is that the asthenosphere is a region where plumes hotter than the average mantle spread below the lithosphere, forming a global pool of elevated temperatures with a negative thermal gradient at its base explaining the gradual increase of seismic velocities at ~ 250–350 km depth (Cammarano et al., 2009).

The above three hypotheses of asthenospheric origin are not necessarily contradictory, because they focus on different geophysical observations: i) The lithosphere-asthenosphere boundary (LAB), indicated in the oceanic plates at the depths ~ 70 km by the drop in wavespeed, could be related to a change in the water content, ii) The receiver-function data at ~ 150 km depth (Hua et al., 2023) could be sensitive to a widespread onset of the first-stage, low degree partial melting, iii) The yet deeper increase of seismic velocities at ~ 250 – 350 km depth could be linked with a negative thermal gradient resulting from accumulation of hot material from mantle plumes in the sublithospheric region.

ORCID(s): 0000-0002-3413-6120 (V. Patočka)

45 Geodynamic significance of the asthenosphere, i.e. that
46 on geological timescales, is in transferring stresses to/from
47 tectonic plates (Forsyth and Uyeda, 1975; Coltice et al.,
48 2019). The lateral extent of some of the major tectonic plates
49 largely exceeds the depth of the mantle, indicating a long-
50 wavelength mantle convection flow (Su and Dziewonski,
51 1992; Hager and Richards, 1989; Richards and Engebretson,
52 1992). Such a large aspect ratio cells are, however, theo-
53 retically unstable at Earth's Rayleigh number (Busse, 1985;
54 Turcotte and Schubert, 1982) – a viscosity contrast between
55 the asthenosphere and the underlying mantle is required in
56 order to stabilize these long-wavelength structures (Bunge
57 et al., 1996; Ahmed and Lenardic, 2010; Busse et al., 2006;
58 Lenardic et al., 2006).

59 Lenardic et al. (2019) argue that plate tectonics is a self-
60 sustaining system whose components: the asthenosphere,
61 subducting slabs, and long-wavelength flow are mutually
62 interdependent. Subduction of large tectonic plates generates
63 an asymmetry between the convective velocity of down- and
64 up-flows, which in turn results in a sub-adiabatic thermal
65 gradient in Earth's mantle (Busse, 1985; Jeanloz and Morris,
66 1987). This, together with the pressure dependence of vis-
67 cosity, increases the viscosity contrast between the upper and
68 the lower mantle – a necessary ingredient for channelization
69 of horizontal mantle flow and thus for reducing the otherwise
70 destabilizing horizontal drag at the base of large tectonic
71 plates. The system of feedbacks and loops is analyzed in a
72 number of studies (see references in Lenardic et al., 2019)
73 and many of them neglect dislocation creep in the mantle.

74 All the above studies argue that the asthenosphere is
75 of thermal and/or compositional origin. Here we explore
76 sublithospheric weakening due to dislocation creep at the
77 base of subducting plates, activated by the high strain-rates

78 that result from the relative motion of oceanic plates and the
79 underlying mantle (dynamically generated asthenosphere).

80 The idea that dislocation creep is important in the shal-
81 low mantle is not new. In fact, until the 90s dislocation creep
82 was thought to dominate over diffusion creep throughout the
83 entire upper mantle (e.g. Carter and Ave'Lallemant, 1970;
84 Green and Radcliffe, 1972). Karato and Wu (1993) then
85 argued that dislocation creep is localised only in the astheno-
86 sphere while the cold and shallow and the deeper mantle
87 deform via diffusion creep. Dislocation creep is also the
88 main candidate for generating a lattice preferred orientation
89 in minerals and is thus commonly used in interpreting seis-
90 mic anisotropy, which is strongest near athenospheric depths
91 (e.g. Debayle et al., 2005; Becker et al., 2014; Walpole et al.,
92 2017).

93 In geodynamic modelling on a regional scale, dislocation
94 creep is also a typical ingredient, promoting strain-rates in
95 regions of high stresses, enhancing velocities (van den Berg
96 et al., 1993) and facilitating motion of the stiff subducting
97 plates (e.g. Billen and Hirth, 2007; Chertova et al., 2012;
98 Yang et al., 2018; Pokorný et al., 2021; Cerpa et al., 2022).
99 Despite these frequent links between dislocation creep and
100 the sublithospheric mantle, the stress-induced (dynamic)
101 contribution of Earth's asthenosphere has not been glob-
102 ally quantified. Dynamic asthenosphere is considered in the
103 works of Semple and Lenardic (2018, 2020, 2021), but their
104 numerical models employ an idealized, layered viscosity
105 structure with activation parameters smaller compared to the
106 experimental values. Moreover, the asthenospheric viscosity
107 reduction is quantified only in the last of these works (Sem-
108 ple and Lenardic, 2021), where a conceptually different,
109 stagnant lid model is investigated, in which weakening is
110 a result of high strain-rates in a convecting layer below an
111 immobile lithosphere (similarly in Schulz et al., 2020).

112 Mantle viscosity is a key to understanding fundamental
 113 Earth science questions and numerous studies attempted to
 114 infer it from a wide variety of data. Primary constraints were
 115 obtained from the inversions of Earth’s geoid (e.g. Hager
 116 et al., 1985; Hager and Richards, 1989; Ricard et al., 1993)
 117 and postglacial rebound (e.g. Peltier, 1998; Mitrovica and
 118 Forte, 2004), and from laboratory experiments of pressur-
 119 ized rocks (e.g. Karato, 2008). Most studies have consid-
 120 ered only radially dependent (i.e., 1D) viscosity structure,
 121 and yet wide-ranging estimates of viscosity profiles have
 122 been obtained. Richards and Lenardic (2018) noted that the
 123 mismatch in the asthenosphere might be caused by the fact
 124 that the long-wavelength geoid and postglacial rebound are
 125 both sensitive to a combination of the viscosity contrast
 126 between the asthenosphere and underlying mantle and the
 127 asthenospheric thickness (Cathles parameter) rather than to
 128 the actual value of viscosity in the asthenosphere.

129 After inversions aiming at the radial viscosity structure,
 130 efforts have been invested in inferring also the lateral vis-
 131 cosity variations (LVV) in some parts of the mantle, espe-
 132 cially the asthenosphere. Čadek and Fleitout (2003) have
 133 demonstrated that the viscosity below the oceanic plates is
 134 by 2 orders of magnitude weaker than the deep continental
 135 roots. Yang and Gurnis (2016) and Mao and Zhong (2021)
 136 assume weak plate margins in their inversions, but do not
 137 consider dislocation creep at the base of tectonic plates.
 138 Yang and Gurnis (2016) include high-accuracy residual
 139 topography measurements into the fitted data and obtain
 140 asthenospheric LVV much smaller than those predicted by
 141 forward models with laboratory-based activation parameters
 142 of diffusion creep – suggesting that some weakening mech-
 143 anism is missing around the cold and stiff subducting slabs
 144 in their models. Mao and Zhong (2021) use weak plate mar-
 145 gins in their convection model to obtain surface velocities

consistent with the present-day plate motions. In order to
 match the toroidal component of the surface velocity field,
 they need to lower the resistance of the circum-pacific plate
 margin significantly with respect to other plate margins, but a
 physical reason for such an ad-hoc manipulation is not clear.

Subduction controls the distribution and fragmentation
 of Earth’s tectonic plates (Mallard et al., 2016). Slab dy-
 namics are therefore an important and somewhat indepen-
 dent indicator of the mantle viscosity structure. In the past,
 subduction models have been used to infer the upper to
 lower mantle viscosity ratio (Čížková et al., 2012; Liu et al.,
 2021). Here we estimate the laterally dependent contribution
 of dislocation creep to sublithospheric weakening, without
 arguing against thermal and/or compositional effects – the
 different weakening mechanisms are likely superimposed
 in the real Earth. We assume that the dynamic weakening
 stems from the shear of mobile tectonic plates with re-
 spect to the underlying mantle. Slab pull on the subducted
 part of the lithospheric plates drives plate motion which
 in turn reinforces asthenospheric weakening in a dynamic
 feedback through nonlinear dislocation creep. We employ
 numerical models of subduction that include diffusion and
 dislocation creep with laboratory based parameters (Hirth
 and Kohlstedt, 2003), and study the relation between plate
 velocity and asthenospheric weakening. By comparing this
 relation with the current plate motions, we finally estimate
 dynamically generated weakening and the resulting lateral
 viscosity variations (LVV) in the asthenosphere.

2. Subduction models

We perform two families of “generic” subduction mod-
 els, meaning that the initial and boundary conditions are
 not tailored to any specific geographic location. The model
 setup and parameters are similar to those used in previous

179 studies (Čížková and Bina, 2019) and are listed in Table 1. In
 180 one family of models, the overriding plate is attached to the
 181 right boundary, mimicking Earth’s regions with stationary
 182 trench and little to no motion of the overriding plate. In these
 183 models, denoted as “fixed OP”, the trench rollback does not
 184 occur. In the second family of models, labelled as “mobile
 185 OP”, a mid ocean ridge is imposed at the right top boundary.
 186 In this setup OP is free to move trenchwards and thus can
 187 accomodate trench rollback. We note that OP is strong and
 188 does not allow for horizontal extension, therefore rollback of
 189 the SP is associated with the motion of OP as a whole.

190 Within each family of models, the individual simulations
 191 differ by the initial age of the subducting plate, ranging from
 192 50 to 150 Myr at the trench (Table 1). Subduction evolution
 193 is evaluated in an extended Boussinesq model that includes
 194 buoyancy and latent heat effects of major mantle phase
 195 transitions at 410 km and 660 km depths (e.g. Pokorný et al.,
 196 2023). A composite rheological model combines diffusion
 197 creep, dislocation creep and power-law stress limiter. An
 198 effective viscosity of the upper mantle and transition zone
 199 is calculated as

$$\eta_{\text{eff}} = \left(\frac{1}{\eta_{\text{diff}}} + \frac{1}{\eta_{\text{disl}}} + \frac{1}{\eta_y} \right)^{-1}. \quad (1)$$

201 The viscosity of diffusion creep is evaluated as

$$\eta_{\text{diff}} = A_{\text{diff}}^{-1} \exp\left(\frac{E_{\text{diff}} + pV_{\text{diff}}}{RT}\right), \quad (2)$$

203 where A_{diff} is pre-exponential parameter, E_{diff} is activation
 204 energy, p is lithostatic pressure, V_{diff} is activation volume of
 205 diffusion creep, R is the gas constant and T is temperature.

206 Dislocation creep viscosity is

$$\eta_{\text{disl}} = A_{\text{disl}}^{-1/n} \mathbb{D}_{\parallel}^{(1-n)/n} \exp\left(\frac{E_{\text{disl}} + pV_{\text{disl}}}{nRT}\right), \quad (3)$$

208 where A_{disl} , E_{disl} and V_{disl} are the pre-exponential paramete-
 209 ter, activation energy, and activation volume of dislocation
 210 creep, \mathbb{D}_{\parallel} is the second invariant of the strain rate tensor, and
 211 the exponent $n = 3.5$ (Kameyama et al., 1999). Finally the
 212 power-law stress limiter viscosity is

$$\eta_y = \sigma_y \mathbb{D}_y^{-(1/n_y)} \mathbb{D}_{\parallel}^{(1/n_y)-1} \quad (4) \quad 213$$

214 where \mathbb{D}_y is the reference strainrate, σ_y is the yield stress and
 215 the power-law exponent is taken as $n_y = 10$.

216 Activation parameters based on experimental data for
 217 wet olivine are assumed in the upper mantle and the tran-
 218 sition zone (Hirth and Kohlstedt, 2003). We note that our
 219 activation energy of dislocation creep is in the range indi-
 220 cated also by van Hunen et al. (2005) to fit the seismically
 221 inferred thermal structure of the Pacific lithosphere. In the
 222 lower mantle we assume diffusion creep with parameters
 223 based on Čížková et al. (2012). Duration of each simulation
 224 is 100 Myr.

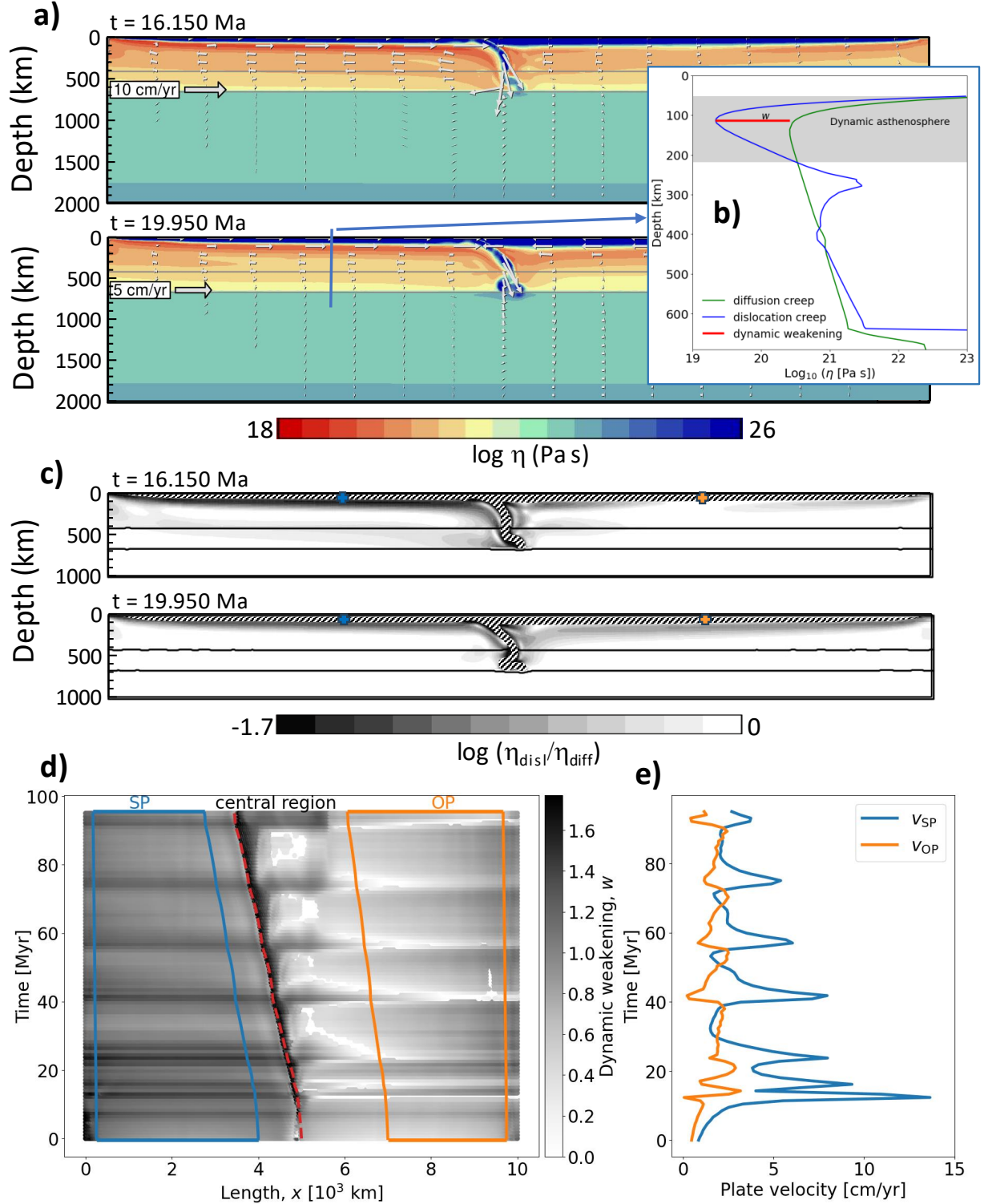


Figure 1: a) Effective viscosity η_{eff} in model M4 (Table 1) for two snapshots in time ($t = 16.15$ and 19.95 Myr). b) Profile of diffusion and dislocation creep viscosity along a selected vertical line. Dynamic asthenosphere is marked in grey color, the amplitude of dynamic weakening w is marked in red, cf. Eq. (5). c) Ratio of dislocation to diffusion creep viscosity in the upper mantle for the same snapshots as in panel a. Blue and orange crosses depict tracers, placed inside the lithosphere, that are used to evaluate v_{SP} and v_{OP} respectively. Crosshatched regions mark the SP and OP. d) Spatio-temporal evolution of dynamic weakening in model M4. Red dashed line marks the position of the trench, x_T , blue and orange lines indicate the length extent over which w is averaged to get $\langle w \rangle$. e) Temporal evolution of subducting (v_{SP}) and overriding (v_{OP}) plate velocities in the same model (M4).

Table 1
 Model parameters

Symbol	Meaning	Value	Units
Upper mantle and oceanic lithosphere rheology			
A_{diff}	Pre-exponential parameter of diffusion creep ^a	1×10^{-9}	$Pa^{-1} s^{-1}$
A_{dist}	Pre-exponential parameter of dislocation creep ^a	31.5×10^{-18}	$Pa^{-n} s^{-1}$
E_{diff}	Activation energy of diffusion creep ^a	3.35×10^5	$J mol^{-1}$
E_{dist}	Activation energy of dislocation creep ^a	4.8×10^5	$J mol^{-1}$
V_{diff}	Activation volume of diffusion creep ^a	4.0×10^{-6}	$m^3 mol^{-1}$
V_{dist}	Activation volume of dislocation creep ^a	11×10^{-6}	$m^3 mol^{-1}$
n	dislocation creep exponent	3.5	–
D_y	Reference strain rate	1×10^{-15}	s^{-1}
σ_y	Stress limit	2×10^8	Pa
n_y	Stress limit exponent	10	–
R	Gas constant	8.314	$J K^{-1} mol^{-1}$
Lower mantle rheology			
A_{diff}	Pre-exponential parameter of diffusion creep	1.3×10^{-16}	$Pa^{-1} s^{-1}$
E_{diff}	Activation energy of diffusion creep ^b	2×10^5	$J mol^{-1}$
V_{diff}	Activation volume of diffusion creep ^b	1.1×10^{-6}	$m^3 mol^{-1}$
Other model parameters			
L, D	Model domain dimensions (length, depth)	$10^4, 2 \cdot 10^3$	km
κ	Thermal diffusivity	10^{-6}	$m^2 s^{-1}$
g	Gravitational acceleration	9.8	$m^2 s^{-2}$
ρ_0	Reference density	3416	$kg m^{-3}$
c_p	Specific heat	1250	$J kg^{-1} K^{-1}$
α_0	Surface thermal expansivity	3×10^{-5}	K^{-1}
γ_{410}	Clapeyron slope of 410 km phase transition ^c	2×10^6	$Pa K^{-1}$
γ_{660}	Clapeyron slope of 660 km phase transition ^c	-2.5×10^6	$Pa K^{-1}$
$\delta_{\rho 410}$	Density contrast of 410 km phase transition ^d	273	$kg m^{-3}$
$\delta_{\rho 660}$	Density contrast of 660 km phase transition ^d	341	$kg m^{-3}$
Description of different models			
Label	Initial age of SP	Initial age of OP	Ridge in the right top corner?
M1	50 Myr	100 Myr	No (fixed OP)
M2	100 Myr	100 Myr	No (fixed OP)
M3	150 Myr	100 Myr	No (fixed OP)
M4	50 Myr	100 Myr	Yes (mobile OP)
M5	100 Myr	100 Myr	Yes (mobile OP)
M6	150 Myr	100 Myr	Yes (mobile OP)
M7	100 Myr	50 Myr	Yes (mobile OP)
M8	100 Myr	150 Myr	Yes (mobile OP)
M9	150 Myr	150 Myr	Yes (mobile OP)

^a Parameters of wet olivine based on Hirth and Kohlstedt (2003)

^b Čížková et al. (2012)

^c Bina and Helffrich (1994)

^d Steinbach and Yuen (1995)

3. Dynamic weakening below the subducting and overriding plates

In both model families, a distinct region forms below the subducting plate (SP), where the viscosity of dislocation creep is smaller than that of diffusion creep. We denote this compact, sub-plate domain where $\eta_{\text{disl}} < \eta_{\text{diff}}$ as the “dynamic asthenosphere” (or simply the asthenosphere in the following text). We define the dynamic weakening w as

$$w(x, t) = \log \frac{\min(\eta_{\text{disl}})}{\min(\eta_{\text{diff}})}, \quad (5)$$

(cf. also Fig. 1b). The quantity w is a measure of the viscosity reduction that is caused by the high strain-rate below the plate (or by the high stress – note that dislocation creep viscosity can be formulated either as a function of strain-rate or as a function of stress (van den Berg et al., 1993)). At each time t for each horizontal position x , the minima in Eq. (5) are found over the entire domain depth. In Fig. 1d, we show how w is distributed both horizontally and temporarily in model M4.

The value of w is approximately constant up to $x \approx 0.8 x_T$, where x_T is the (time varying) position of the trench. In subsequent analysis, we will represent the dynamic weakening below the SP with the value of w averaged over $x \in (0.05, 0.8) x_T$ to avoid regions near the plate boundaries (ridge and trench) which are dominated by vertical flow (discussion of the near-trench region follows at the end of this section).

As the subducting slab starts sinking into the mantle, its velocity v_{SP} varies due to the increasing slab pull, varying resistance of the mantle and petrological buoyancy associated with the phase transitions (Fig. 1e). First, the plate speeds up as the 410 km phase transition enhances the slab pull, then it slows down in response to the 660 km phase

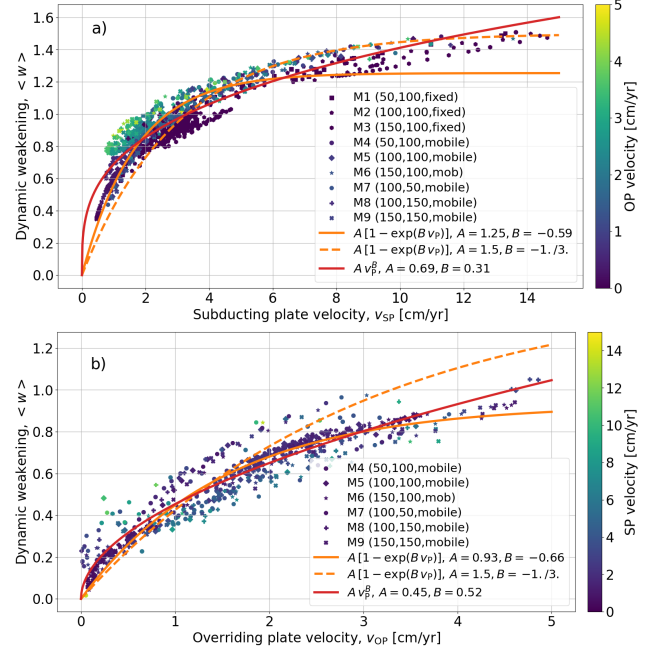


Figure 2: a) Dynamic weakening w below the SP, averaged over the segment $x \in (0.05x_T, 0.8x_T)$ (cf. the blue segment in Fig. 1d), plotted as a function of the SP velocity v_{SP} . Different symbols represent different models (Table 1), color marks the OP velocity v_{OP} in each respective snapshot in time. Orange curve shows the best fit of the data using Eq. (6), dashed line is the parametrization that we employ in Fig. 3. b) Dynamic weakening below the OP (orange segment in Fig. 1d). Color marks the SP velocity v_{SP} .

transition and to the viscosity increase in the lower mantle. In later stages, variations of plate velocity are driven by slab buckling (Čížková and Bina, 2013).

We assume that the magnitude of strain-rate in the asthenosphere is primarily controlled by the contrast of plate velocity with respect to the underlying mantle and therefore aim to derive a relation between dynamic weakening and plate velocity. Fig. 2a shows that the plate velocity v_{SP} provides a primary control on the dynamic weakening below the SP, because the same trend is observed for all the models, i.e. regardless of the initial plate age. The data indicate first a steep increase of $\langle w \rangle$ with v_{SP} , and then the slope decreases when plate velocity is higher. We choose a two parameter fit using an exponential function,

$$f(v_p) = A \cdot (1 - \exp(B \cdot v_p)) \quad (6)$$

272 where v_P is the plate velocity in cm/yr ($v_P = v_{SP}$ in Fig. 2a
 273 and $v_P = v_{OP}$ in Fig. 2b). Simultaneous fit of the data from
 274 all the performed simulations gives $A = 1.25$ and $B = 0.59$
 275 below SP, root mean square error of the fit is 0.09.

276 In the family of fixed OP models, dynamic weakening is
 277 measured only below the SP. In mobile OP models, a similar
 278 effect is observed and measured also below the overriding
 279 plate. In Fig. 2b, we plot $\langle w \rangle$ evaluated below the OP as a
 280 function of the rollback velocity, v_{OP} . The weakening below
 281 OP is represented by an average value of w over the segment
 282 $(x - x_T)/(L - x_T) \in (0.4, 0.95)$, with L denoting the length
 283 of the model, $L = 10^4$ km (see the orange segment in
 284 Fig. 1d).

285 Similarly to SP (Fig. 2), also under OP the dependence
 286 of dynamic weakening on the plate velocity is comparable
 287 in all the investigated models, implying that the $\langle w \rangle(v_P)$
 288 scaling law, Eq. (6), is applicable to a generic subduction
 289 setting. The dynamic weakening is, however, less spatially
 290 uniform below OP when compared to SP (see Fig. 1d),
 291 with w slightly increasing toward the right edge, making
 292 the average value $\langle w \rangle$ somewhat dependent on the x -range
 293 over which the average is computed. Nevertheless, in first ap-
 294 proximation, the asthenosphere below OP can be represented
 295 with the same $\langle w \rangle(v_P)$ relationship as the asthenosphere
 296 below SP (cf. the orange dashed line in Fig. 2).

297 The color of symbols in Fig. 2 marks the complementary
 298 plate velocity. Fig. 2a shows that dynamic weakening below
 299 SP is enhanced when OP velocity is high, while dynamic
 300 weakening below OP seems to be slightly reduced for most
 301 data points with a high v_{SP} , with the exception of when OP
 302 is nearly stagnant ($v_{OP} < 1$ cm/yr). This behaviour is related
 303 to the interplay between the two plates during buckling.

304 The subducting plate velocity, v_{SP} , undergoes quasi-
 305 periodic variations (described in more detail in e.g. Čížková

and Bina (2013)). In the episodes of fast v_{SP} when the dip
 306 angle of the slab increases, there is a negligible rollback and
 307 OP is more less stagnant. Below SP is a return flow (Fig. 1a)
 308 whose strength, and thus the amplitude of dynamic weaken-
 309 ing, is governed entirely by v_{SP} at this stage of subduction.
 310 Weakening of the mantle wedge is also dominated by v_{SP}
 311 during this stage, because the fast-sinking slab weakens the
 312 mantle at its base and above its upper surface. The overriding
 313 plate velocity, v_{OP} is typically small when v_{SP} is large, and
 314 dynamic weakening below OP is also small (Fig. 1d).
 315

316 In a complementary stage, typically when a large seg-
 317 ment of the slab encounters an increased resistance at the 660
 318 km phase transition, v_{SP} decreases and low dip angle results
 319 in a fast rollback episode accompanied by an increase of the
 320 rollback velocity (Fig. 1e). The strength of return flow below
 321 SP is partly governed by how fast the SP is 'laying flat',
 322 which is, however, related to the rollback velocity, v_{OP} . This
 323 explains why the data points in Fig. 2a that correspond to
 324 time steps with a high v_{OP} (bright color) show above average
 325 weakening. At this stage, v_{OP} is relatively large, and the
 326 mantle wedge is dominated by the flow below the OP, which
 327 has the same direction as that of the plate and magnitude
 328 decreasing with depth (Couette flow).

329 As a result, dynamic weakening above the already flat-
 330 lying slab shows a more complicated pattern and is cyclically
 331 governed by either v_{SP} or v_{OP} . This is a natural consequence
 332 of the fact that the central region (Fig. 1d) progressively
 333 contains both the SP and OP, which disrupts the simple
 334 relation between asthenospheric viscosity and the surface
 335 velocity described by Eq. (6). We exclude the central region
 336 from the analysis in Fig. 2.

337 Nevertheless, Eq. (6) provides a reasonable first-order
 338 estimate for the global distribution of the dynamic weak-
 339 ening w . In the next section, we apply the formula $w =$
 340 $1.5 [1 - \exp(-v_p/3)]$ to estimate LVV below Earth's oceans.

341 Both below the SP and OP, the dynamic asthenosphere
 342 has an average central depth of ca. 150 km, and is ca. 200
 343 km thick (cf. the grey area in Fig. 1b), which agrees with the
 344 common definition of asthenosphere that is based on seismic
 345 and electromagnetic sounding observations.

346 4. Dynamic LVV

347 Inferring mantle viscosity from geophysical observa-
 348 tions is a tedious but important task. The available data
 349 are insufficient to perform a 3D inversion without making
 350 additional simplifying assumptions (e.g. Čadek and Fleitout,
 351 2003). One way to move forward is to improve our a priori
 352 knowledge of LVV in the mantle. In this section, we use
 353 the empirical law, Eq. (6), to make a first-order estimate of
 354 LVV in the asthenosphere from reconstructed values of the
 355 absolute surface plate motions (Müller et al., 2019) (Fig. 3).

356 Using Eq. (6) globally is based on two simplifying
 357 assumptions. First, we assume that subduction dynamics
 358 dominates asthenospheric flow below the oceans. Coltice
 359 et al. (2019) evaluated the areal fraction F_D of the surface
 360 that is dragged by the interior in global mantle convection
 361 models with imposed continents. The average value of F_D
 362 was about 35% in their simulations, with the continental ar-
 363 eas contributing to F_D proportionally more than the oceans.
 364 Their results imply that the surface plates are the main
 365 driver of the interior in oceanic regions, consistently with
 366 our approach. Second, we apply Eq. (6) to the entire area
 367 of oceanic plates, while the central and ridge regions were
 368 excluded from the analysis in Fig. 2 (cf. Fig. 1d).

369 Despite these crude simplifications, the dynamic LVV
 370 predicted in Fig. 3 naturally explain several observations and
 371 help in resolving some problems experienced in previously
 372 published viscosity inversions. First of all, the dynamic
 373 weakening below the oceans is likely to be significantly
 374 larger than below the continents. While we restrict our
 375 analysis to oceans only, it can be expected that dynamic
 376 weakening below the continents is much smaller, because
 377 the drift of continents is on average much slower than the
 378 average velocity of oceanic plates (e.g. Torsvik et al., 2008).
 379 This result is in line with the findings of Ricard et al. (1991)
 380 and Čadek and Ricard (1992), who analyze the net rota-
 381 tion of the lithosphere (degree one toroidal velocities) and
 382 conclude that “asthenospheric viscosity below the oceans is
 383 at least one order of magnitude lower than underneath the
 384 continents”, consistently with later geoid inversions (Čadek
 385 and Fleitout, 2003).

386 Secondly, the pacific plate is moving fast and thus is
 387 most lubricated. In order to match the present-day global
 388 surface velocities, Mao and Zhong (2021) had to reduce the
 389 resistance of the circum-pacific plate margin by a factor of
 390 ca. 7 with respect to other plate margins. However, if the
 391 asthenospheric LVV as predicted in Fig. 3 were accounted
 392 for in their study, such an ad hoc reduction would not
 393 be necessary – the surface velocities of the pacific plate
 394 would increase even if the resistance of the circum-pacific
 395 plate margin was the same as the resistance of other plate
 396 margins. There are two dominant mechanisms that control
 397 the surface velocity of a plate: the resistance at its margin,
 398 and the friction at its base. The horizontal drag at the base of
 399 the pacific plate is significantly smaller than in most other
 400 regions (Fig. 3), which may allow for its relatively large
 401 surface velocity without the circum-pacific margin's resis-
 402 tance being smaller when compared to other plate margins.

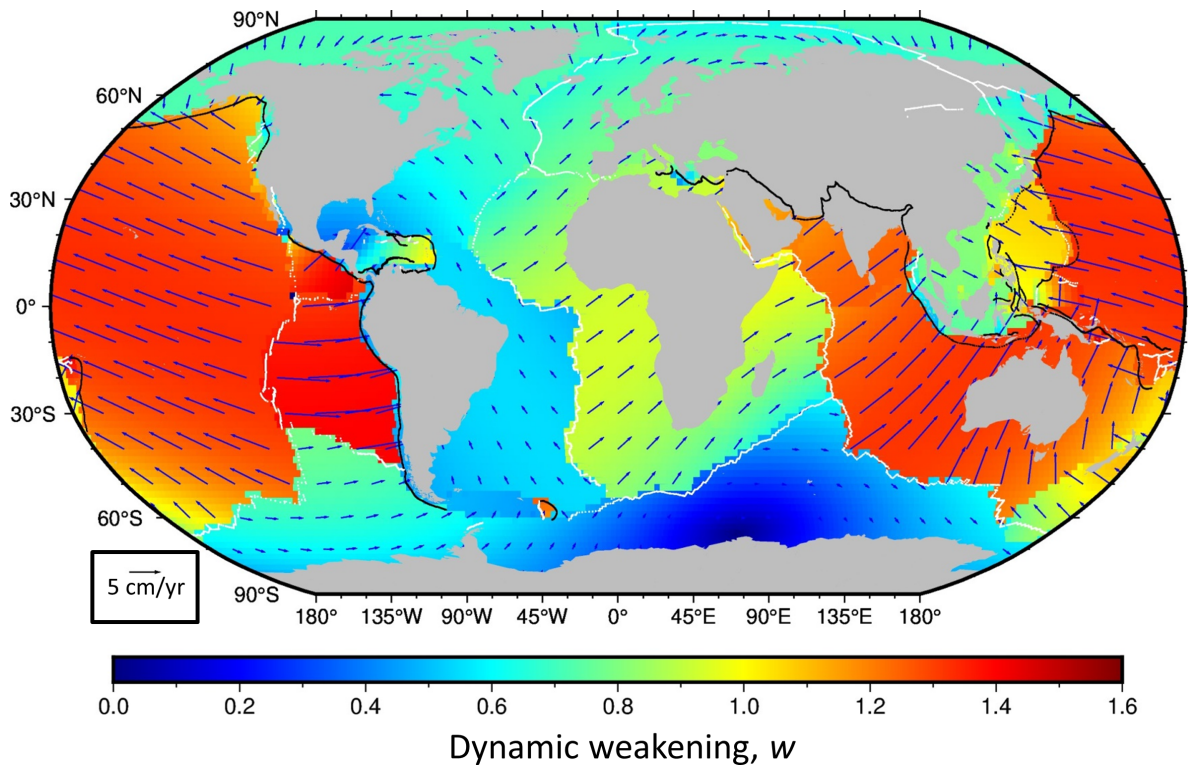


Figure 3: Dynamic weakening below Earth's oceanic plates. Vectors show the absolute plate velocities derived by Müller et al. (2019), obtained with a freely available software package GPlates (Boyden et al., 2011). Sublithospheric dynamic weakening, w , showed in color, is computed from these velocities using our empirical law, $w = 1.5 [1 - \exp(-v_p/3)]$. The quantity w represents a first-order estimate of the LVV in the asthenosphere. Grey areas depict Earth's continents, black and white lines show the major trenches and ridges, respectively (Coffin, 1998).

403 Note also that the surface plate velocities by Müller et al.
 404 (2019) are computed such as to minimize the net lithospheric
 405 rotation. In reference frames that allow for faster net rotation
 406 rates, the westward velocities of plates increase (Doglioni
 407 et al., 2015). In this regard, the speed of the Pacific plate in
 408 Fig. 3 is the bottom estimate.

409 Finally, the oldest and thus coldest slabs sink at the
 410 fastest rates. Our results therefore suggest that, at large
 411 wavelengths, the viscosity variations resulting from temper-
 412 ature effects should be partly compensated by the dynamic
 413 weakening. This is in line with the fact that the inverted
 414 long-wavelength LVV (e.g. Yang and Gurnis, 2016) are
 415 much smaller than those predicted by forward models using
 416 laboratory-based constitutive relations for diffusion creep,
 417 in which the variations are suggested to be at least several
 418 orders of magnitude (e.g. Stadler et al., 2010).

5. Discussion and conclusions 419

420 We have evaluated the sublithospheric viscosity of dis-
 421 location and diffusion creep in a number of free subduction
 422 simulations. There is a significant dynamic weakening be-
 423 low both the subducting and the overriding plate, and it is
 424 primarily controlled by the amplitude of the surface velocity.

425 Given the importance of asthenosphere in the plate tec-
 426 tonics theory, our results warn against the use of numerical
 427 simulations with only diffusion creep. In a series of papers
 428 summarized by Lenardic et al. (2019), the viscosity contrast
 429 between the asthenosphere and the underlying mantle is
 430 linked with a sub-adiabatic temperature profile that results
 431 from an asymmetry between up- and down-wellings. Here,
 432 we show that a significant viscosity contrast may result sim-
 433 ply from the relative motion of tectonic plates with respect
 434 to the underlying mantle.

435 The mutual feedback between plate velocities and their
 436 basal lubrication is likely to play a role during tectonic
 437 history of Earth. A drawback of the exponential law, Eq.(6),
 438 is its quick saturation, resulting in an underestimation of
 439 dynamic weakening when plate velocities are higher than
 440 ca. 20 cm/yr (based on additional simulations not shown
 441 here). In order to predict dynamic weakening in episodes of
 442 rapid plate motions, that is, for a broader range of v_p , we
 443 find that power-law is more suitable ($\langle w \rangle = A v_p^B$ gives a
 444 comparable fit also in the here studied range of v_p , see the
 445 red solid line in Fig. 2).

446 The volume fraction of partial melt is likely less than
 447 0.1% away from mid ocean ridges (e.g. Karato, 2012),
 448 and the presence of the 150-km (i.e. the first-stage melt-
 449 ing) boundary showed no correlation with radial seismic
 450 anisotropy, indicating that partial melt has no substantial
 451 effect on the large-scale viscosity of the asthenosphere
 452 (Hua et al., 2023). Increased water content or elevated
 453 temperatures due to the accumulation of plume material are,
 454 however, likely to produce additional, significant LVV in
 455 Earth’s upper mantle. It is important to stress that we do not
 456 argue against the presence of partial melt, variations in the
 457 water content, or pooling of plume material in Earth’s upper
 458 mantle.

459 The presence or absence of asthenosphere is often de-
 460 bated in the context of Venus (e.g. Pauer et al., 2006).
 461 Recently, Maia et al. (2023) performed a global inversion
 462 of Venus’s geoid and topography using a Bayesian inference
 463 approach. They inferred a ~ 235 km thin, low-viscosity zone
 464 with a viscosity reduction of 5–15 times with respect to the
 465 underlying mantle. Given the different tectonic regime of
 466 Earth and Venus, a less pronounced asthenosphere on Venus
 467 is consistent with dynamic weakening being a significant,
 468 but not the sole mechanism involved.

There is a notable difference between the sublithospheric
 flow structure in our models when compared to typical
 global models (e.g. Lenardic et al., 2019; Coltice et al.,
 2019). While in the global models, Couette or Poiseuille
 flow dominates below the oceanic plates (i.e. plates drag
 the interior or the interior drags the surface plates), in our
 simulations, which contain more realistic slab dynamics, the
 sublithospheric mantle is driven by the return flow below
 the sinking slab (Fig. 1a, the return flow is confined in the
 upper mantle). In this particular aspect, our simulations are
 similar to those presented by Morgan et al. (2013), who show
 that bulk of the asthenosphere resists being dragged down
 at the subduction zone (cf. their Fig. 1 and Section 2.3).
 They argue that grid resolution of 4 km is needed to capture
 this behaviour, far less than in typical global simulations.
 Note, however, that when slab penetrates into the lower
 mantle, which happens in models with fixed overriding plate,
 a whole-mantle convection cell develops below the SP. In
 our case, the return flow in the upper mantle is thus related
 to the folding of the slab in the transition zone rather than
 to the return of anomalously hot material as in Morgan
 et al. (2013). Note also that Fig. 2a contains data from
 all our simulations over the entire simulation time (100
 Myr), indicating that the scaling law in Eq. (6) captures the
 behaviour both before and after the penetration of the slab
 into the lower mantle.

On the other hand, regional modelling suffers from the
 intrinsic incapability to capture how local dynamics af-
 fect the global flow structure, which in turn determines
 the boundary conditions of regional-scale models. To fully
 reconcile the above discrepancy, one must perform global
 numerical simulations with grid resolution of present-day
 regional models – a challenging task. In one case or the
 other, strain rates are likely to be high below the fast moving

503 tectonic plates, and we show that dynamic weakening due
 504 to dislocation creep is an important mechanism under such
 505 conditions, significantly contributing to the formation of the
 506 low-viscosity asthenosphere.

507 6. Acknowledgements

508 We thank Arie van den Berg for discussions on the
 509 nonlinear rheology of upper mantle and Wim Spakman for
 510 sharing his script for viscosity/velocity plots. This work
 511 has been supported by Charles University Research Centre
 512 program No. UNCE/24/SCI/005.

513 Open Research

514 The viscosity fields, interpolated onto a regular grid, and
 515 the time evolution of plate velocities in all models, as well as
 516 scripts that were used to produce Fig. 1b,c,d,e and Fig. 2 are
 517 available at Zenodo (Patočka, 2024). Figure 1a was produced
 518 using the python interface for the Generic Mapping Tool
 519 (pyGMT) software (<https://pypi.org/search/?q=pygmt>).

520 CRedit authorship contribution statement

521 **Vojtěch Patočka:** Conceptualization, Methodology, In-
 522 vestigation, Visualization, Writing - Original draft prepara-
 523 tion. **Hana Čížková:** Conceptualization, Investigation, Vi-
 524 sualization, Writing - Review & Editing. **Jakub Pokorný:**
 525 Investigation, Visualization, Writing - Review & Editing.

526 References

527 Ahmed, O., Lenardic, A., 2010. Low viscosity channels and the stability
 528 of long wavelength convection. *Phys. Earth Planet. Inter.* 179, 122–126.
 529 doi:10.1016/j.pepi.2010.01.008.
 530 Barrell, J., 1914. The strength of the earth's crust. *The Journal of Geology*
 531 22, 655–683. doi:10.1086/622181.
 532 Becker, T.W., Conrad, C.P., Schaeffer, A.J., Lebedev, S., 2014. Origin
 533 of azimuthal seismic anisotropy in oceanic plates and mantle. *Earth*
 534 *Planet. Sci. Lett.* 401, 236–250. doi:10.1016/j.epsl.2014.06.014.

van den Berg, A., van Keken, P., Yuen, D., 1993. The effects of a com- 535
 posite non-newtonian and newtonian rheology on mantle convection. 536
Geophys. J. Int. , 62–78. 537
 Billen, M., Hirth, G., 2007. Rheologic controls on slab dynamics. 538
Geochem. Geophys. Geosyst. 8, Q08012. doi:10.1029/2007GC001597. 539
 Bina, C.R., Helffrich, G., 1994. Phase transition Clapeyron slopes and tran- 540
 sition zone seismic discontinuity topography. *Journal of Geophysical* 541
Research: Solid Earth 99, 15853–15860. doi:10.1029/94JB00462. 542
 Boyden, J.A., Müller, R.D., Gurnis, M., Torsvik, T.H., Clark, J.A., Turner, 543
 M., Ivey-Law, H., Watson, R.J., Cannon, J.S., 2011. Next-generation 544
 plate-tectonic reconstructions using gplates . 545
 Bunge, H., Richards, M., Baumgardner, J., 1996. Effect of depth-dependent 546
 viscosity on the planform of mantle convection. *Nature* 379, 436–438. 547
 doi:10.1038/379436a0. 548
 Busse, F., Richards, A., Lenardic, A., 2006. A simple model of high prandtl 549
 and high rayleigh number convection bounded by thin low-viscosity 550
 layers. *Geophys. J. Int.* 164, 160–167. doi:10.1111/j.1365-246X.2005. 551
 02836.x. 552
 Busse, F.H., 1985. Transition to turbulence in Rayleigh-Beénard con- 553
 vection. Springer Berlin Heidelberg, Berlin, Heidelberg. pp. 97– 554
 137. URL: [https://doi.org/10.1007/](https://doi.org/10.1007/3-540-13319-4_15) 555
[3-540-13319-4_15](https://doi.org/10.1007/3-540-13319-4_15), doi:10.1007/ 556
[3-540-13319-4_15](https://doi.org/10.1007/3-540-13319-4_15). 557
 Cammarano, F., Romanowicz, B., Stixrude, L., Lithgow-Bertelloni, C., Xu, 558
 W., 2009. Inferring the thermochemical structure of the upper mantle 559
 from seismic data. *Geophys. J. Int.* 179, 1169–1185. doi:10.1111/j. 560
 1365-246X.2009.04338.x. 561
 Carter, N., Ave'Lallemant, H., 1970. High Temperature Flow of Dunite and 562
 Peridotite. *GSA Bulletin* 81, 2181–2202. doi:10.1130/0016-7606(1970) 563
 81[2181:HTFODA]2.0.CO;2. 564
 Cerpa, N.G., Sigloch, K., Garel, F., Heuret, A., Davies, Rhodri, D., Miha- 565
 lynuk, M.G., 2022. The effect of a weak asthenospheric layer on surface 566
 kinematics, subduction dynamics and slab morphology in the lower 567
 mantle. *J. Geophys. Res.* , e2022JB024494doi:10.1029/2022JB024494. 568
 Chertova, M., Geenen, T., van den Berg, A., Spakman, W., 2012. Using 569
 open sidewalls for modelling self-consistent lithosphere subduction dy- 570
 namics. *Solid Earth* , 313–326doi:10.5194/se-3-313-2012. 571
 Coffin, M., 1998. Present-day plate boundary digital data compilation. 572
 University of Texas Institute for geophysics technical report 174, 5. 573
 Coltice, N., Husson, L., Faccenna, C., Arnould, M., 2019. What drives 574
 tectonic plates? *Sci. Advances* 5. doi:10.1126/sciadv.aax4295.

- 575 Debayle, E., Kennett, B., Priestley, K., 2005. Global azimuthal seismic
576 anisotropy and the unique plate-motion deformation of australia. NA-
577 TURE 433, 509–512. doi:10.1038/nature03247. 616
- 578 Doglioni, C., Carminati, E., Crespi, M., Cuffaro, M., Penati, M., Riguzzi,
579 F., 2015. Tectonically asymmetric earth: From net rotation to polarized
580 westward drift of the lithosphere. *Geoscience Frontiers* 6, 401–418.
581 doi:10.1016/j.gsf.2014.02.001. 617
- 582 Dziewonski, A., Anderson, D., 1981. Preliminary reference earth model.
583 *Phys. Earth Planet. Inter.* 25, 297–356. doi:10.1016/0031-9201(81)
584 90046-7. 618
- 585 Forsyth, D., Uyeda, S., 1975. Relative importance of driving forces of plate
586 motion. *Geophys. J. Royal Astro. Soc.* 43, 163–200. doi:10.1111/j.
587 1365-246X.1975.tb00631.x. 619
- 588 Green, H., Radcliffe, S., 1972. Dislocation mechanisms in olivine and flow
589 in the upper mantle. *Earth Planet. Sci. Lett.* 15, 239–247. doi:10.1016/
590 0012-821X(72)90169-0. 620
- 591 Hager, B., Clayton, R., Richards, M., Comer, R., Dziewonski, A., 1985.
592 Lower mantle heterogeneity, dynamic topography and the geoid. *Nature*
593 313, 541–546. doi:10.1038/313541a0. 621
- 594 Hager, B., Richards, M., 1989. Long-wavelength variations in
595 earth's geoid - physical models and dynamical implications. *Phi-
596 los. Trans. R. Soc. London* 328, 309–327. doi:10.1098/rsta.1989.0038. 622
- 597 Hirschmann, M.M., 2010. Partial melt in the oceanic low velocity zone.
598 *Phys. Earth Planet. Inter.* 179, 60–71. doi:10.1016/j.pepi.2009.12.003. 623
- 599 Hirth, G., Kohlstedt, D., 2003. Rheology of the upper mantle and the mantle
600 wedge: A view from the experimentalists. *Inside the subduction factory,*
601 *Geophysical monograph* 138 doi:10.1029/138GM06. 624
- 602 Hua, J., Fischer, K.M., Becker, T.W., Gazel, E., Hirth, G., 2023. As-
603 thenospheric low-velocity zone consistent with globally prevalent partial
604 melting. *Nat. Geo* doi:10.1038/s41561-022-01116-9. 625
- 605 van Hunen, J., Zhong, S., Shapiro, N.M., Ritzwoller, M.H., 2005. New
606 evidence for dislocation creep from 3-d geodynamic modeling of the
607 pacific upper mantle structure. *Earth Planet. Sci. Lett.* , 146–155doi:10.
608 1016/j.epsl.2005.07.006. 626
- 609 Jeanloz, R., Morris, S., 1987. Is the mantle geotherm subadiabatic.
610 *Geophys. Res. Lett.* 14, 335–338. doi:10.1029/GL014i004p0335. 627
- 611 Kameyama, M., Yuen, D., Karato, S., 1999. Thermal-mechanical effects of
612 lowtemperature plasticity (the peierls mechanism) on the deformation of
613 a viscoelastic shear zone. *Earth Planet. Sci. Lett.* , 159–172. 628
- 614 Karato, S., Wu, P., 1993. Rheology of the upper mantle - a synthesis.
615 *Science* 260, 771–778. doi:10.1126/science.260.5109.771. 629
- Karato, S.i., 2008. Insights into the nature of plume-asthenosphere interac-
tion from central pacific geophysical anomalies. *Earth Planet. Sci. Lett.*
274, 234–240. doi:10.1016/j.epsl.2008.07.033. 630
- Karato, S.i., 2012. On the origin of the asthenosphere. *Earth
Planet. Sci. Lett.* 321, 95–103. doi:10.1016/j.epsl.2012.01.001. 631
- Kawakatsu, H., Kumar, P., Takei, Y., Shinohara, M., Kanazawa, T., Araki,
E., Suyehiro, K., 2009. Seismic evidence for sharp lithosphere-
asthenosphere boundaries of oceanic plates. *SCIENCE* 324, 499–502.
doi:10.1126/science.1169499. 632
- Lambert, I., Wyllie, P., 1970. Low-velocity zone of earths mantle - incipient
melting caused by water. *Science* 169, 764+. doi:10.1126/science.169.
3947.764. 633
- Lenardic, A., Richards, M.A., Busse, F.H., 2006. Depth-dependent rhe-
ology and the horizontal length scale of mantle convection. *J. Geo-
phys. Res. Sol. Earth* 111. doi:10.1029/2005JB003639. 634
- Lenardic, A., Weller, M., Hoink, T., Seales, J., 2019. Toward a boot strap hy-
pothesis of plate tectonics: Feedbacks between plates, the asthenosphere,
and the wavelength of mantle convection. *Phys. Earth Planet. Inter.* 296.
doi:10.1016/j.pepi.2019.106299. 635
- Liu, H., Gurnis, M., Leng, W., 2021. Constraints on mantle viscosity
from slab dynamics. *J. Geophys. Res. Sol. Earth* 126. doi:10.1029/
2021JB022329. 636
- Maia, J.S., Wieczorek, M.A., Plesa, A.C., 2023. The mantle viscosity
structure of venus. *Geophys. Res. Lett.* 50, e2023GL103847. doi:10.
1029/2023GL103847. 637
- Mallard, C., Coltice, N., Seton, M., Muller, R.D., Tackley, P.J., 2016. Sub-
duction controls the distribution and fragmentation of earth's tectonic
plates. *Nature* 535, 140+. doi:10.1038/nature17992. 638
- Mao, W., Zhong, S., 2021. Constraints on mantle viscosity from
intermediate-wavelength geoid anomalies in mantle convection models
with plate motion history. *J. Geophys. Res. Sol. Earth* 126. doi:10.1029/
2020JB021561. 639
- Mierdel, K., Keppler, H., Smyth, J.R., Langenhorst, F., 2007. Water solubil-
ity in aluminous orthopyroxene and the origin of earth's asthenosphere.
Science 315, 364–368. doi:10.1126/science.1135422. 640
- Mitrovica, J., Forte, A., 2004. A new inference of mantle viscosity based
upon joint inversion of convection and glacial isostatic adjustment data.
Earth Planet. Sci. Lett. 225, 177–189. doi:10.1016/j.epsl.2004.06.005. 641
- Montagner, J., Tanimoto, T., 1991. Global upper mantle tomography of
seismic velocities and anisotropies. *J. Geophys. Res. Sol. Earth* 96,
20337–20351. doi:10.1029/91JB01890. 642

- 657 Morgan, J., Morgan, W., 1999. Two-stage melting and the geochemical
658 evolution of the mantle: a recipe for mantle plum-pudding. *Earth*
659 *Planet. Sci. Lett.* 170, 215–239.
- 660 Morgan, J.P., Hasenclever, J., Shi, C., 2013. New observational and
661 experimental evidence for a plume-fed asthenosphere boundary layer in
662 mantle convection. *Earth Planet. Sci. Lett.* 366, 99–111. doi:10.1016/j.
663 epsl.2013.02.001.
- 664 Müller, R.D., Zahirovic, S., Williams, S.E., Cannon, J., Seton, M., Bower,
665 D.J., Tetley, M.G., Heine, C., Le Breton, E., Liu, S., Russell, S.H.J.,
666 Yang, T., Leonard, J., Gurnis, M., 2019. A global plate model including
667 lithospheric deformation along major rifts and orogens since the triassic.
668 *Tectonics* 38, 1884–1907. doi:10.1029/2018TC005462.
- 669 Patočka, V., 2024. Simulation data for manuscript Dynamic component of
670 the asthenosphere: lateral viscosity variations due to dislocation creep at
671 the base of oceanic plates. doi:10.5281/zenodo.10499016.
- 672 Pauer, M., Fleming, K., Cadek, O., 2006. Modeling the dynamic component
673 of the geoid and topography of venus. *J. Geophys. Res. Planets* 111.
674 doi:10.1029/2005JE002511.
- 675 Peltier, W., 1998. Postglacial variations in the level of the sea: Implications
676 for climate dynamics and solid-earth geophysics. *Rev. Geophys.* 36,
677 603–689. doi:10.1029/98RG02638.
- 678 Pokorný, J., Čížková, H., Bina, C., van den Berg, A., 2023. 2d stress
679 rotation in the tonga subduction region. *Earth Planet. Sci. Lett.* ,
680 118379doi:10.1016/j.epsl.2023.118379.
- 681 Pokorný, J., Čížková, H., van den Berg, A., 2021. Feedbacks between
682 subduction dynamics and slab deformation: Combined effects of non-
683 linear rheology of a weak decoupling layer and phase transitions.
684 *Phys. Earth Planet. Inter.* doi:10.1016/j.pepi.2021.106679.
- 685 Ricard, Y., Doglioni, C., Sabadini, R., 1991. Differential rotation between
686 lithosphere and mantle - a consequence of lateral mantle viscosity
687 variations. *J. Geophys. Res.* 96, 8407–8415. doi:10.1029/91JB0204.
- 688 Ricard, Y., Richards, M., Lithgow-Bertelloni, C., Lestunff, Y., 1993.
689 A geodynamic model of mantle density heterogeneity. *J. Geo-*
690 *phys. Res. Sol. Earth* 98, 21895–21909. doi:10.1029/93JB02216.
- 691 Richards, M., Engebretson, D., 1992. Large-scale mantle convection and
692 the history of subduction. *Nature* 355, 437–440. doi:10.1038/355437a0.
- 693 Richards, M.A., Lenardic, A., 2018. The cathles parameter (ct): A
694 geodynamic definition of the asthenosphere and implications for the
695 nature of plate tectonics. *Geochem. Geophys. Geosyst.* 19, 4858–4875.
696 doi:10.1029/2018GC007664.
- Rychert, C.A., Shearer, P.M., 2009. A global view of the lithosphere-
asthenosphere boundary. *Science* 324, 495–498. doi:10.1126/science.
1169754.
- Schulz, F., Tosi, N., Plesa, A.C., Breuer, D., 2020. Stagnant-lid convection
with diffusion and dislocation creep rheology: Influence of a non-
evolving grain size. *Geophys. J. Int.* 220, 18–36. doi:10.1093/gji/ggz417.
- Semple, A., Lenardic, A., 2020. The robustness of pressure-driven as-
thenospheric flow in mantle convection models with plate-like behavior.
Geophys. Res. Lett. 47. doi:10.1029/2020GL089556.
- Semple, A.G., Lenardic, A., 2018. Plug flow in the earth's asthenosphere.
Earth Planet. Sci. Lett. 496, 29–36. doi:10.1016/j.epsl.2018.05.030.
- Semple, A.G., Lenardic, A., 2021. Feedbacks between a non-newtonian
upper mantle, mantle viscosity structure and mantle dynamics. *Geo-*
phys. J. Int. 224, 961–972. doi:10.1093/gji/ggaa495.
- Shankland, T., O'Connell, R., Waff, H., 1981. Geophysical constraints
on partial melt in the upper mantle. *Rev. Geophys.* 19, 394–406.
doi:10.1029/RG019i003p00394.
- Stadler, G., Gurnis, M., Burstedde, C., Wilcox, L.C., Alisic, L., Ghattas, O.,
2010. The dynamics of plate tectonics and mantle flow: From local to
global scales. *Science* 329, 1033–1038. doi:10.1126/science.1191223.
- Steinbach, V., Yuen, D.A., 1995. The effects of temperature-dependent
viscosity on mantle convection with the two major phase transitions.
Physics of the Earth and Planetary Interiors 90, 13 – 36. doi:10.1016/
0031-9201(95)03018-R.
- Su, W., Dziewonski, A., 1992. On the scale of mantle heterogeneity.
Phys. Earth Planet. Inter. 74, 29–54. doi:10.1016/0031-9201(92)90066-5.
- Torsvik, T.H., Müller, R.D., Van der Voo, R., Steinberger, B., Gaina, C.,
2008. Global plate motion frames: Toward a unified model. *Reviews of*
Geophysics 46. doi:10.1029/2007RG000227.
- Turcotte, D.L., Schubert, G., 1982. *Geodynamics*. John Wiley and Sons,
New York. pp. 134–159.
- Čadek, O., Fleitout, L., 2003. Effect of lateral viscosity variations in the
top 300 km on the geoid and dynamic topography. *Geophys. J. Int.* 152,
566–580. doi:10.1046/j.1365-246X.2003.01859.x.
- Čadek, O., Ricard, Y., 1992. Toroidal poloidal energy partitioning and
global lithospheric rotation during cenozoic time. *Earth Planet. Sci. Lett.*
109, 621–632. doi:10.1016/0012-821X(92)90120-K.
- Čížková, H., van den Berg, A.P., Spakman, W., Matyska, C., 2012. The vis-
cosity of earth's lower mantle inferred from sinking speed of subducted
lithosphere. *Phys. Earth Planet. Inter.* 200, 56–62. doi:10.1016/j.pepi.
2012.02.010.

- 738 Čížková, H., Bina, C., 2013. Effects of mantle and subduction-interface
739 rheologies on slab stagnation and trench rollback. *Earth Planet. Sci. Lett.*
740 , 95–103doi:10.1016/j.epsl.2013.08.011.
- 741 Čížková, H., Bina, C., 2019. Linked influences on slab stagnation: Interplay
742 between lower mantle viscosity structure, phase transitions, and plate
743 coupling. *Earth Planet. Sci. Lett.* , 88–99doi:10.1016/j.epsl.2018.12.
744 027.
- 745 Walpole, J., Wookey, J., Kendall, J.M., Masters, T.G., 2017. Seis-
746 mic anisotropy and mantle flow below subducting slabs. *Earth*
747 *Planet. Sci. Lett.* 465, 155–167. doi:10.1016/j.epsl.2017.02.023.
- 748 Yang, T., Gurnis, M., 2016. Dynamic topography, gravity and the role
749 of lateral viscosity variations from inversion of global mantle flow.
750 *Geophys. J. Int.* 207, 1186–1202. doi:10.1093/gji/ggw335.
- 751 Yang, T., Moresi, L., Zhao, D., Sandiford, D., Whittaker, J., 2018. Cenozoic
752 lithospheric deformation in northeast asia and the rapidly-aging pacific
753 plate. *Earth Planet. Sci. Lett.* doi:10.1016/j.epsl.2018.03.057.